MICROBIOLOGY

Helicity-directed recognition of bacterial phospholipid via radially amphiphilic antimicrobial peptides

Yangbin Liang[1,2]†, Yuhao Zhang[1,2]†, Yu Huang[3]†, Cheng Xu[4]†, Jingxian Chen[1,2], Xinshuang Zhang[1,2], Bingchuan Huang[1,2], Zhanhui Gan[5], Xuehui Dong[5], Songyin Huang[6], Chengrun Li[1,2], Shuyi Jia[1,2], Pengfei Zhang[1], Yueling Yuan[1,7], Houbing Zhang[1], Yucai Wang[8], Bing Yuan[4], Yan Bao[9]*, Shiyan Xiao[3]*, Menghua Xiong[1,2]*

The fundamental differences in phospholipids between bacterial and mammalian cell membranes present remarkable opportunities for antimicrobial design. However, it is challenging to distinguish bacterial anionic phospholipid phosphatidylglycerol (PG) from mammalian anionic phosphatidylserine (PS) with the same net charge. Here, we report a class of radially amphiphilic α helix antimicrobial peptides (RAPs) that can selectively discriminate PG from PS, relying on the helix structure. The representative RAP, L_{10}-MMBen, can direct the rearrangement of PG vesicles into a lamellar structure with its helix axis parallel to the PG membrane surface. The helical structure imparts both the thermodynamic and kinetic advantages of L_{10}-MMBen/PG assembly, and the hiding of hydrophobic regions in RAPs is crucial for PG recognition. L_{10}-MMBen exhibits high selectivity against bacteria depending on PG recognition, showing low in vivo toxicity and significant treatment efficacy in mice infection models. Our study introduces a helicity-direct bacterial phospholipid recognition paradigm for designing highly selective antimicrobial peptides.

INTRODUCTION

Antimicrobial peptides (AMPs), with common cationic and amphipathic features, are prone to interact with and destroy the negatively charged phospholipid bilayer of bacterial membranes mainly through electrostatic and hydrophobic interactions, showing great potential for combating drug resistant bacteria (*1*–*7*). Numerous natural AMPs and their synthetic mimics have been developed and optimized (*8*–*19*), but, because of their nonspecific toxicity to mammalian cells, their clinical applications are now limited to mainly topical administration, such as with the skin and nasal and oral cavities (*20*–*22*).

The antibacterial selectivity of cationic AMPs is mainly attributed to the highly negative charge of bacterial membranes, which are rich in anionic phosphatidylglycerol (PG; ~20 to 90% of the total phospholipids), cardiolipin (CL; ~5% of the total phospholipids), and lipopolysaccharides (LPSs; for Gram-negative bacteria) (*23*). The cationic and hydrophobic groups, as well as their amphiphilic balance and spatial distribution, are considered essential ingredients for optimizing AMPs to exhibit potent bactericidal activity and low toxicity toward mammalian cells (*24*–*29*). However, mammalian plasma membranes also contain a significant amount of anionic phospholipids, particularly phosphatidylserine (PS; ~15% of the total phospholipids) that have an electrostatic interaction with cationic AMPs (*30*). Moreover, the hydrophobic fragments of amphipathic AMPs induce nonspecific hydrophobic interactions with the amphipathic lipids in mammalian cells. Thus, with the inherent characteristic of anionic and amphipathic of mammalian cell membranes, the nonspecific toxicity of AMPs against mammalian cells seems to be inevitable in the simple model of electrostatic and hydrophobic interactions.

Phospholipids differ considerably between bacterial membranes and mammalian cell membranes (*6*, *31*). Besides the zwitterionic phosphoethanolamine (PE) that is present in both mammalian and bacterial membranes, bacterial membranes contain a high level of anionic phospholipid PG, whereas mammalian plasma membranes contain zwitterionic phosphocholine (PC) and sphingomyelin (SM), as well as anionic phospholipid PS (*32*, *33*). PG plays a pivotal role in enhancing membrane stability, governing lipid packing and acyl chain arrangement of phospholipids, and modulating membrane permeability (*34*). Therefore, bacteria-specific phospholipid PG could be a promising target in designing antimicrobials. However, the challenge lies in distinguishing PG from PS, which have the same net charge.

Here, we report on a class of bacterial phospholipid PG recognizing radially amphiphilic AMPs (RAPs). RAPs were constructed by elongating charge-containing amino acid side chains to position the charges distally from the polypeptide backbone, a modification that has been reported to produce water-soluble, ultra-stable α-helical peptides (*16*, *35*). RAPs feature a hydrophobic helical core surrounded by cationic groups in all radial directions of the helix,

[1]School of Biomedical Sciences and Engineering, South China University of Technology, Guangzhou International Campus, Guangzhou 511442, P. R. China. [2]National Engineering Research Centre for Tissue Restoration and Reconstruction, South China University of Technology, Guangzhou 510006, P. R. China. [3]CAS Key Laboratory of Soft Matter Chemistry, Department of Polymer Science and Engineering, Hefei National Laboratory for Physical Sciences at Microscale, University of Science and Technology of China, Hefei, Anhui 230026, P. R. China. [4]Songshan Lake Materials Laboratory, Institute of Physics, Chinese Academy of Sciences, Dongguan, 523808, P. R. China. [5]South China Advanced Institute for Soft Matter Science and Technology, School of Emergent Soft Matter, South China University of Technology, Guangzhou 510640, China. [6]Biotherapy Center, Sun Yat-Sen Memorial Hospital, Sun Yat-Sen University, Guangzhou, 510120, P. R. China. [7]Key Laboratory of Biomedical Materials and Engineering of the Ministry of Education, South China University of Technology, Guangzhou, Guangdong 510006, P. R. China. [8]Division of Molecular Medicine, Hefei National Laboratory for Physical Sciences at Microscale, the CAS Key Laboratory of Innate Immunity and Chronic Disease, School of Life Sciences, University of Science and Technology of China, Hefei, Anhui, 230027, P. R. China. [9]Guangdong Provincial Key Laboratory of Malignant Tumor Epigenetics and Gene Regulation, Guangdong-Hong Kong Joint Laboratory for RNA Medicine, Medical Research Center, Sun Yat-Sen Memorial Hospital, Sun Yat-Sen University, Guangzhou 510120, P. R. China.
*Corresponding author. Email: xiongmh@scut.edu.cn (M.X.); xiaosy@ustc.edu.cn (S.X.); baoy5@mail.sysu.edu.cn (Y.B.)
†These authors contributed equally to this work.

contrasting with natural AMPs, which typically have cationic and hydrophobic amino acids separated onto opposite faces of the helix (*16*). A series of RAPs were synthesized by modification of the side chains with quaternary ammonium groups (R) of varying hydrophobicity (Fig. 1A). Through isothermal titration calorimeter (ITC) assessment, we found that RAPs have the ability to selectively discriminate PG from both the main anionic phospholipid PS and zwitterionic phospholipids (PC, PE, and SM) present in mammalian membranes. The representative peptide L_{10}-MMBen can direct the rearrangement of PG vesicles into a lamellar structure with the helix axis of the peptide parallel to the PG membrane surface according to small-angle x-ray scattering (SAXS), cryo–transmission electron microscopy (cryo-TEM), and single-molecule fluorescence imaging. We revealed that the helical structure is crucial for PG recognition of L_{10}-MMBen and imparts both thermodynamic and kinetic advantages to L_{10}-MMBen/PG assembly as indicated by coarse-grained (CG) molecular dynamic (MD) simulations. Furthermore, we found that the hiding of hydrophobic domains in the radially amphiphilic structure is an important factor for PG recognition. PG recognition endows the RAPs with highly selective membranolytic activity against bacteria. L_{10}-MMBen exhibited >1000-fold higher antimicrobial activity and greater selectivity against bacteria in comparison to the corresponding disordered DL_{10}-MMBen peptide, which has the same chemical composition, net charge, and hydrophobicity but does not recognize PG. The treatment with L_{10}-MMBen showed low in vivo toxicity and significantly reduced the bacterial burden in the bladders of a bladder infection model. In addition, it significantly increased the survival rate of mice in a polymicrobial sepsis model induced by cecal ligation and puncture (CLP). Our study introduces an approach to design bacterial phospholipid recognizing AMPs.

RESULTS

RAPs selectively recognize bacterial phospholipid PG

We constructed a series of helical RAPs (L_{10}-R) containing various quaternary ammonium groups (R) (Fig. 1A). These AMPs were synthesized through *N*-carboxyanhydride (NCA) polymerization and quaternary aminations with aliphatic tertiary amines, including *N*,*N*-dimethylbutylamine (MMB), *N*,*N*-dimethylhexylamine (MMH), and *N*,*N*-dimethyloctylamine (MMO), as well as aromatic tertiary amine *N*,*N*-dimethylbenzylamine (MMBen) (scheme S1 and fig. S1) (*16*). The degree of polymerization (DP) for these peptides is 10. L_{10}-R adopted an α-helical structure with a helicity of ~50% in aqueous solutions, as indicated by the circular dichroism (CD) spectra (Fig. 1, B and C). The helical structure of L_{10}-R was further verified by Fourier transform infrared spectrometer, exhibiting strong amide I band at 1653 cm^{-1} and amide II band at 1547 cm^{-1} (fig. S2). These RAPs displayed excellent helical stability against elevated temperature and against helix-destabilizing reagents such as high concentrations of NaCl and urea (fig. S3).

To screen bacterial phospholipids targeting peptides, we evaluated the interaction between L_{10}-R and the main phospholipids present in the bacterial membrane (PG and PE) and in mammalian membranes (PS, PC, SM, and PE) by ITC (Fig. 1D). Phospholipids with unsaturated (DO and PO series) and saturated (DP series) hydrophobic tails were tested (Fig. 1D). L_{10}-R interacted with all tested PGs obviously [1,2-dioleoyl-*sn*-glycero-3-phospho-(1′-rac-glycerol) (DOPG), 1-palmitoyl-2-oleoyl-*sn*-glycero-3-phospho-(1′-rac-glycerol) (POPG), and 1,2-dipalmitoyl-*sn*-glycero-3-phospho-(1′-rac-glycerol) (DPPG)] but showed no apparent interaction with zwitterionic phospholipids, including PC, PE, and SM (Fig. 1E, fig. S4, and table S2). For PS, L_{10}-R exhibited an interaction with unsaturated 1,2-dioleoyl-*sn*-glycero-3-phospho-L-serine (DOPS) and 1-palmitoyl-2-oleoyl-*sn*-glycero-3-phospho-L-serine (POPS) but showed no apparent interaction with saturated 1,2-dipalmitoyl-*sn*-glycero-3-phospho-L-serine (DPPS) except L_{10}-MMO with highly hydrophobic quaternary ammonium groups (Fig. 1E and fig. S4). L_{10}-R exhibited a stronger interaction with PG than PS having the same net charge and lipid tails (Fig. 1, F to H, and table S2). In particular, we identified L_{10}-MMBen as the top selective RAP exhibiting a 14.2- and 9.3-fold stronger interaction with unsaturated POPG and DOPG than that of POPS and DOPS with the same lipid tails, respectively (Fig. 1, F and G), and L_{10}-MMBen exhibited a strong interaction with saturated DPPG [association constant (Ka) = 0.20 μM^{-1}] but no obvious interaction with saturated DPPS (Fig. 1H and table S2). L_{10}-MMBen also exhibited a strong interaction with 1,2-dilauroyl-*sn*-glycero-3-phospho-(1′-rac-glycerol) (DLPG) (Ka = 10.0 μM^{-1}) with short saturated lipid tails but showed a weaker interaction with LPSs (Ka = 0.035 μM^{-1}) and CL (Ka = 0.10 μM^{-1}) (Fig. 1I and table S3). Notably, the interaction between L_{10}-R and PG was an endothermic and entropic process [both change in enthalpy (ΔH) and change in entropy (ΔS) > 0], indicating that this process is entropy driven (tables S2 and S3).

The stronger interaction between L_{10}-MMBen and the POPG bilayer over POPS was further quantitively measured by using MD simulations. The phospholipids were modeled by using the CG MARTINI v2.2 force field (*36*), and the synthesized peptide force field was parameterized according to the MARTINI rules (figs. S5 to S7 and tables S4 to S6) (*37*). MD simulations that placed the L_{10}-MMBen molecule onto the membrane bilayer suggested that L_{10}-MMBen and POPG achieve a tight interaction, with water molecules located at the contact edge; in contrast, L_{10}-MMBen could not make intimate contact with POPS lipids, and water molecules were observed at the interface between L_{10}-MMBen and POPS lipids (Fig. 1J). A greater number of water molecules and a larger ratio value between water and lipid molecules demonstrated loose contacts between L_{10}-MMBen and the POPS bilayer than those observed with the POPG bilayer (Fig. 1K). The weaker adhesion of L_{10}-MMBen onto the POPS bilayer produces a smaller interaction energy between them (Fig. 1L). The tighter and stronger interactions of POPG with L_{10}-MMBen along with the slightly weaker affinity with water molecules (*38*) may contribute to the higher selectivity of L_{10}-MMBen against bacteria-specific PG phospholipids.

L_{10}-MMBen directs the rearrangement of PG into a lamellar structure

Next, we explored the interaction model of L_{10}-MMBen with PG. Dynamic light scattering was used to monitor the size change of POPG small unilamellar vesicles (SUVs) when titrated with L_{10}-MMBen. Initially, the particle size slowly increased, and the solution gradually became turbid; then, when the molar ratio of peptide to POPG reached ~0.17, the particle size abruptly increased from ~200 to >1000 nm and white precipitate appeared (Fig. 2, A and B). For SUVs prepared with a mixture of POPG and 1,2-dioleoyl-*sn*-glycero-3-phosphocholine (DOPC), the presence of 1-palmitoyl-2-oleoyl-*sn*-glycero-3-phosphocholine (POPC) did not hamper aggregate formation, and the particle size abruptly increased at a similar molar

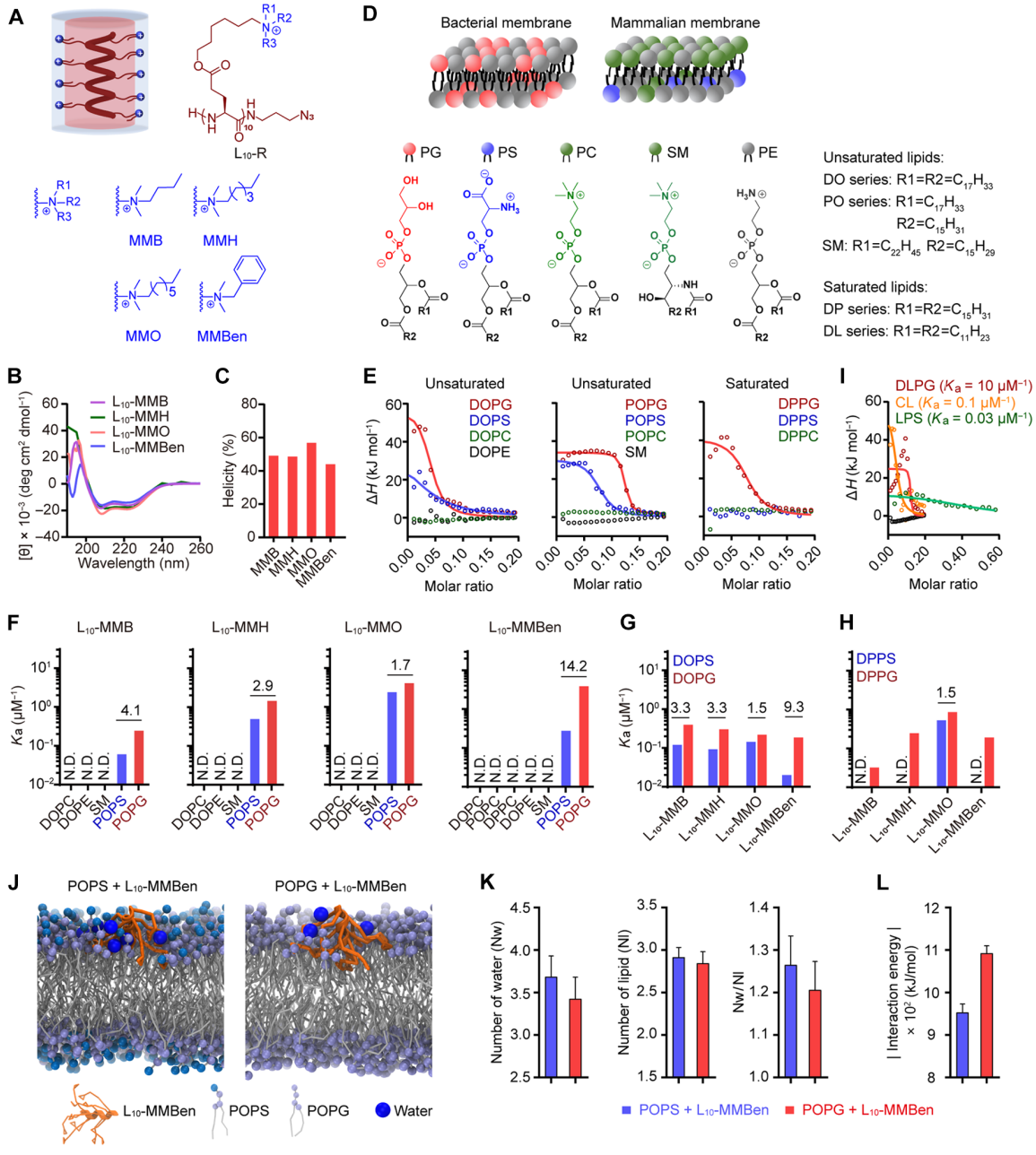

Fig. 1. RAPs selectively recognize bacterial phospholipid PG. (**A**) Schematic illustration of helical L_{10}-R with radial amphiphilicity. R represents the side chain quaternary amine, including *N*,*N*-dimethylbutylamine (MMB), *N*,*N*-dimethylhexylamine (MMH), *N*,*N*-dimethyloctylamine (MMO), and *N*,*N*-dimethylbenzylamine (MMBen). The hydrophobic backbone is colored red, and the cationic quaternary amine is colored blue. CD spectra (**B**) and helicity (**C**) of L_{10}-R in aqueous solution at pH 7.0. (**D**) Schematic illustration of the phospholipid bilayer of bacterial and mammalian cell membranes. PG, PS, PC/SM, and PE are colored in red, blue, green, and gray, respectively. Phospholipids with unsaturated tails (including the DO and PO series) and saturated tails [including the DP series and 1,2-dilauroyl-*sn*-glycero-3-phospho-(1′-rac-glycerol) (DLPG)] were used. (**E**) Isothermal titration calorimeter (ITC)–determined integrated heat release of the interaction between L_{10}-MMBen and phospholipids. L_{10}-MMBen (1.25 mM) was dropped into a phospholipid solution (1.25 mM) in phosphate-buffered saline (PBS) at 25°C. Δ*H*, change in enthalpy. ITC-determined association constant (*Ka*) between L_{10}-R and phospholipids, including 1,2-dioleoyl-*sn*-glycero-3-phosphocholine (DOPC), 1,2-dioleoyl-*sn*-glycero-3-phosphoethanolamine (DOPE), SM, 1-palmitoyl-2-oleoyl-*sn*-glycero-3-phospho-L-serine (POPS), and 1-palmitoyl-2-oleoyl-*sn*-glycero-3-phospho-(1′-rac-glycerol) (POPG) (**F**); 1,2-dioleoyl-*sn*-glycero-3-phospho-L-serine (DOPS) and 1,2-dioleoyl-*sn*-glycero-3-phospho-(1′-rac-glycerol) (DOPG) (**G**); and 1,2-dipalmitoyl-*sn*-glycero-3-phospho-L-serine (DPPS) and 1,2-dipalmitoyl-*sn*-glycero-3-phospho-(1′-rac-glycerol) (DPPG) (**H**). Numbers above the column charts represent multiples of the difference between Ka_{PG} and Ka_{PS}. Ka_{PG} represents the *Ka* value between L_{10}-R and PG, and Ka_{PS} represents the *Ka* value between L_{10}-R and PS. N.D. represents undetectable. (**I**) ITC-determined integrated heat release of the interaction between L_{10}-MMBen and phospholipids (DLPG, LPS, and CL). (**J**) Representative structures for L_{10}-MMBen loading onto the POPS and POPG bilayers. Molecular dynamic (MD) simulations were performed using the Martini coarse-grained (CG) force field. (**K**) The number of water molecules (left) and lipid molecules (middle) lies at the contact area between L_{10}-MMBen and the lipid bilayer, and the number ratio between water and lipid molecules (right). (**L**) Absolute values of interaction energies between L_{10}-MMBen and the phospholipid bilayer. In (K) and (L), data represent average values ± SD derived from 2-μs MD simulations.

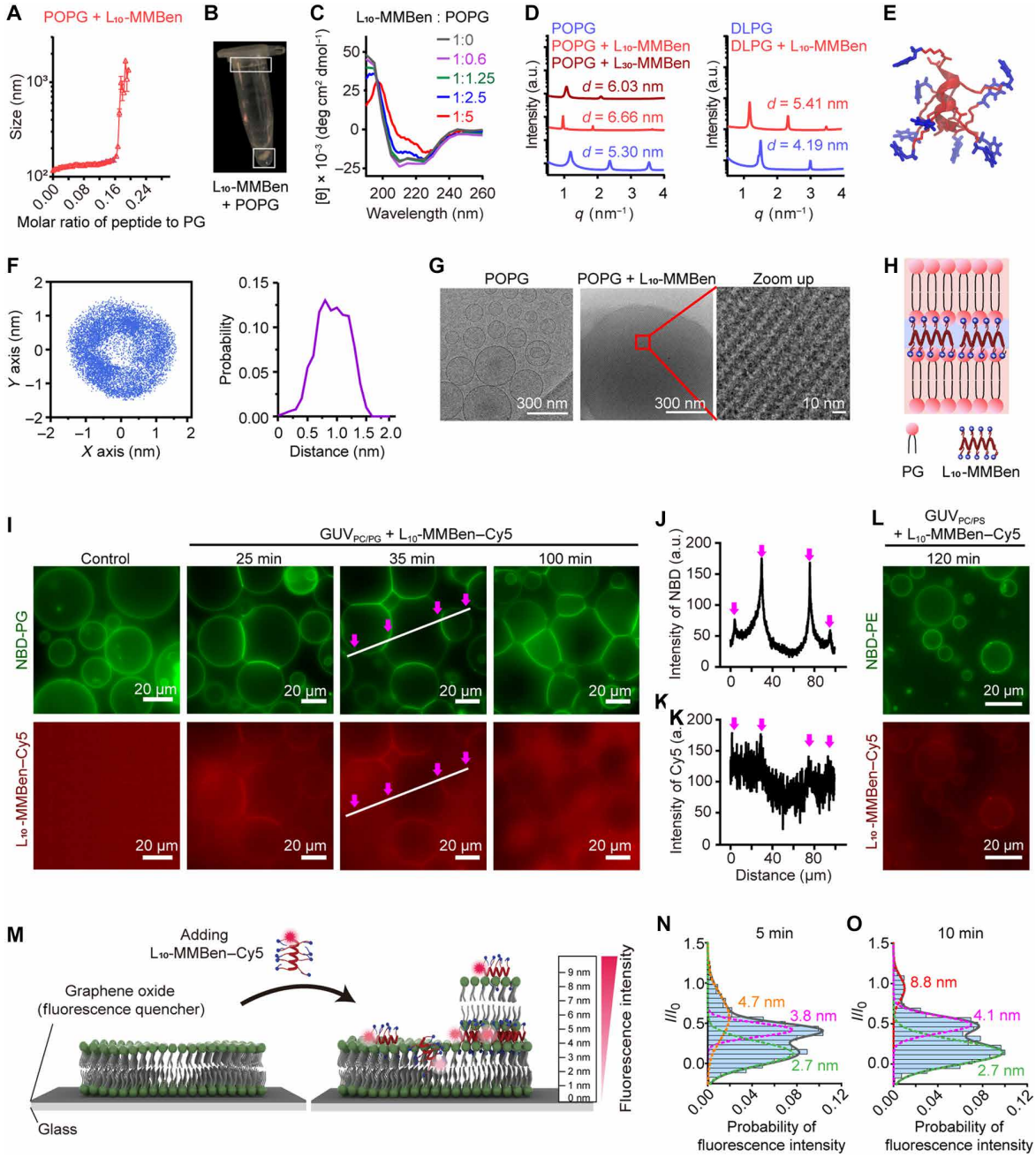

Fig. 2. L_{10}-MMBen directed the rearrangement of PG vesicles into a lamellar structure. (**A**) Size change of POPG vehicles when titrated with L_{10}-MMBen. Data represent average values ± SD ($n = 3$ replicates). (**B**) Image of the aggregates of the L_{10}-MMBen and POPG mixtures. (**C**) CD spectra of L_{10}-MMBen when incubated with different molar ratios of POPG. (**D**) SAXS profiles of L_n-MMBen/POPG aggregates (left) and L_{10}-MMBen/DLPG aggregates (right). (**E**) L_{10}-MMBen structure predicted from all-atom MD simulations. (**F**) Probability distribution of the side-chain N atoms around the helical backbone. (**G**) Cryo-TEM images of POPG vesicles and L_{10}-MMBen/POPG aggregates. Scale bars for images and enlarged images are 300 and 10 nm, respectively. (**H**) Schematic illustration of the lamellar structure of L_{10}-MMBen/PG aggregates. (**I**) Structural illumination microscopy (SIM) images of $GUV_{PC/PG}$ (green) treated with L_{10}-MMBen–Cy5 (red). $GUV_{PC/PG}$ contains DOPC, DOPG, and NBD-PG at a molar ratio of 90:9.9:0.1%. Scale bars, 20 μm. Line-scan profiles of the fluorescence intensity of NBD (**J**) and Cy5 (**K**) after 35 min of incubation. a.u., arbitrary unit. (**L**) SIM images of $GUV_{PC/PS}$ (green) treated with L_{10}-MMBen–Cy5 (red). $GUV_{PC/PS}$ contained DOPC, DOPS, and NBD-PE at a molar ratio of 90:9.9:0.1%. Scale bars, 20 μm. (**M**) Schematic illustration of L_{10}-MMBen–Cy5 induced phospholipid bilayer rearrangement in the SLB system. The SLB comprises 10% DOPG and 90% DOPC and is deposited on a graphene oxide (GO) surface, which works as an energy acceptor plane. The detected Cy5 fluorescence intensity is positively correlated with its distance from the fluorescence quencher-GO surface. The fluorescence of each L_{10}-MMBen–Cy5 molecule was monitored with total internal reflection fluorescence microscopy. Probability distribution of the relative fluorescence intensity (I/I_0) of Cy5 built from ~80 traces in the SLB system treated with L_{10}-MMBen–Cy5 for 5 min (**N**) and 10 min (**O**). The green, purple, orange, and red dashed lines indicate that the metastable positions of the peptide appeared in the vertical direction of SLBs at 2.7, 3.8 to 4.1, 4.7, and 8.8 nm, respectively. I and I_0 represent the detected and pristine fluorescence intensity of L_{10}-MMBen–Cy5, respectively. In (G), representative cryo-TEM images are shown (at least three images per sample). In (I) and (L), representative images from at least two independent experiments are shown.

ratio of peptide to POPG at ~0.16 to 0.17, i.e., one L_{10}-MMBen molecule corresponds to five to six POPG molecules, when the ratio of POPG varied from 90 to 10% (fig. S9, A to E). As a control, the titration of DOPC vesicles with L_{10}-MMBen did not induce the formation of aggregates (fig. S9F).

The microstructure of POPG and L_{10}-MMBen aggregates was then analyzed. When mixed with different ratios of POPG, L_{10}-MMBen retained a helical conformation and the characteristic minima at 222 nm showed a slight redshift when the molar ratio of L_{10}-MMBen:POPG equaled 1:5 (Fig. 2C), which was similar to the reported CD signal of helical peptide aggregates (*39*, *40*). As measured by SAXS, a lamellar structure with a periodicity $d = 6.66$ nm formed in POPG and L_{10}-MMBen aggregates, comparable with $d = 5.30$ nm for POPG vesicles (Fig. 2D). A slightly decreased periodicity ($d = 6.03$ nm) was observed for the POPG and L_{30}-MMBen aggregates. Considering the threefold higher DP, the observed decreased lamellar periodicity implies that the helix axis of the peptide should be parallel to the PG layer (Fig. 2D). When using DLPG with shorter hydrophobic tails than POPG, the periodicity of the DLPG/L_{10}-MMBen lamellar structure decreased to $d = 5.41$ nm (Fig. 2D). The periodicity difference was 1.36 nm between POPG/L_{10}-MMBen and POPG and 1.22 nm between DLPG/L_{10}-MMBen and DLPG, which corresponds approximately to the radial length of L_{10}-MMBen as estimated by theoretical simulation (Fig. 2, E and F). We used cryo-TEM to vividly observe the lamellar structure of the POPG/L_{10}-MMBen aggregates, which had a layer spacing of 5 to 6 nm (Fig. 2G). These results indicated that L_{10}-MMBen and PG organized into a lamellar structure with the helix axis of the peptide parallel to the PG membrane surface (Fig. 2H).

Real-time fluorescence imaging of PG-containing giant unilamellar vesicles (GUVs) and supported lipid bilayers (SLBs) was used to investigate L_{10}-MMBen–induced PG rearrangement. $GUV_{PC/PG}$ containing 0.1% *N*-(7-nitrobenz-2-oxa-1,3-diazole) (NBD)–labeled DOPG (NBD-PG) was used. Structural illumination microscopy observation showed that cyanine5 (Cy5)-labeled L_{10}-MMBen (L_{10}-MMBen–Cy5) induced fusion and deformation of $GUV_{PC/PG}$ (Fig. 2I). In addition, L_{10}-MMBen–Cy5 was colocalized on the fusion interface with NBD-PG (Fig. 2, J and K). Meanwhile, L_{10}-MMBen–Cy5 could not induce fusion or deformation of PS-containing $GUV_{PC/PS}$ in a 120-min incubation (Fig. 2L). In the SLB system, where a phospholipid bilayer comprising DOPG and DOPC (1:9) was deposited on a graphene oxide (GO) surface, single-molecule fluorescence approaches were used to monitor the GO surface-induced fluorescence attenuation of L_{10}-MMBen–Cy5 (Fig. 2M) (*41*). The vertical position of the peptide in SLBs was determined by using the fluorescence intensity of a single L_{10}-MMBen–Cy5 molecule (Fig. 2M) (*41*). At 5 min after coincubation, three metastable positions of L_{10}-MMBen–Cy5 appeared in the vertical direction of SLBs (~4.2-nm thick), which were 2.7, 3.8, and 4.7 nm distant from the substrate (Fig. 2N), indicating the insertion of L_{10}-MMBen–Cy5 into the upper half of the phospholipid membrane and the position of L_{10}-MMBen–Cy5 on the surface of a single phospholipid membrane bilayer. At 10 min, a metastable position appeared 8.8 nm distant from the substrate, which was approximately the thickness of the two bilayer membranes, indicating that SLBs underwent structural recombination to form a double-layer membrane stacked structure (Fig. 2O). Similar to L_{10}-MMBen, L_{10}-MMB, L_{10}-MMH, and L_{10}-MMO also caused the aggregation of PG-containing SUVs (fig. S10A) and induced fusion and deformation of PG-containing GUVs (fig. S10B).

Helicity imparts both thermodynamic and kinetic advantages to the interaction of L_{10}-MMBen/PG

DL_{10}-MMBen, with the same chemical composition, net charge, and hydrophobicity as L_{10}-MMBen but with a disordered structure (figs. S1 and S11A), did not show any apparent interaction with any of the tested phospholipids, including PG (Fig. 3A and table S2) and could not induce the aggregation of PG-containing SUVs and $GUV_{PC/PG}$ (fig. S12, A and B). D_{10}-MMBen, with a helical structure but different chirality (fig. S11B), exhibited a comparable interaction with POPG as observed with L_{10}-MMBen (*Ka* value of ~3.22 μM^{-1}) (Fig. 3B), indicating that the chirality showed an indistinctive effect on the interaction. To study whether the interaction was helicity dependent, we synthesized a series of peptides L_7D_3-MMBen, L_9D_1-MMBen, L_{10}-MMBen, and L_{30}-MMBen, with a helicity of 15.0, 34.3, 47.8, and 53.0%, respectively, by controlling the ratios of D-amino acids and the DP (Fig. 3C, scheme S2, and fig. S1). As the helicity increased, the peptides showed increased interaction with POPG, with *Ka* values of 0.053, 0.95, 3.94, and 15.92 μM^{-1} for L_7D_3-MMBen, L_9D_1-MMBen, L_{10}-MMBen, and L_{30}-MMBen, respectively, as well as enhanced antimicrobial activity (Fig. 3, D and E). These results indicated that the helicity of L_{10}-MMBen impelled its interaction with bacterial anionic PG phospholipid.

CG MD simulations were used to study the mechanism of helicity-directed interaction and assembly between L_{10}-MMBen and PG. Markov state model (*42*, *43*) analysis was applied to extract the quantitative thermodynamic and kinetic information of the assembly of POPG lipids and peptides from MD simulations (fig. S13). The POPG lipids and peptides were initially randomly dispersed and quickly evolved into a metastable crossing-cylinder (CC) state, where the lipids coalesced into arrays of cylindrical micelles (Fig. 3, F and G). The micelle arrays in the CC states were connected by the hydrophobic tails of lipids, achieving a cross-like section, and the peptides were located at the hydrophilic periphery. The CC state was a long-lived metastable kinetic state, with 24.1% of replicas trapped at this state without reaching the final layer-by-layer (LL) state in 12-μs MD simulations for helical L_{10}-MMBen, whereas 51.7% of replicas were trapped at the CC state for disordered DL_{10}-MMBen (Fig. 3H). The CC state could evolve into a metastable porous-rich layer (PrL) state through free energy barriers of 8.08 and 5.93 kJ mol^{-1} for L_{10}-MMBen and DL_{10}-MMBen, respectively (Fig. 3, F and G). Furthermore, a slight barrier of 2.30 kJ mol^{-1} was observed between the PrL and LL states for the α-helical L_{10}-MMBen system, and, by contrast, the disordered DL_{10}-MMBen needed to overcome a much larger barrier of 11.85 kJ mol^{-1} (Fig. 3, F and G). This significant difference explains why LL structures are rarely observed in experiments where POPG was mixed with disordered DL_{10}-MMBen (Fig. 3H). Although POPG lipids mixed with either α helix or disordered polypeptides can assemble into LL structures, the LL structure of POPG lipids with L_{10}-MMBen tightly compacts, whereas that mediated by DL_{10}-MMBen is defective with water pores penetrating across the hydrophilic layers of the POPG head groups (Fig. 3, F and G). In terms of free energy, the LL state is more stable by −4.11 kJ mol^{-1} for POPG mixed with L_{10}-MMBen but is thermodynamically unfavored with a change in Gibbs free energy (ΔG) of 3.92 kJ mol^{-1} for DL_{10}-MMBen compared with the CC state, verifying that LL formation is thermodynamically more favored when POPG assembly is mediated by helical L_{10}-MMBen (Fig. 3, F and G).

Molecular diffusion is a fundamental process underpinning self-assembly (*44*). L_{10}-MMBen diffuses much faster in the POPG

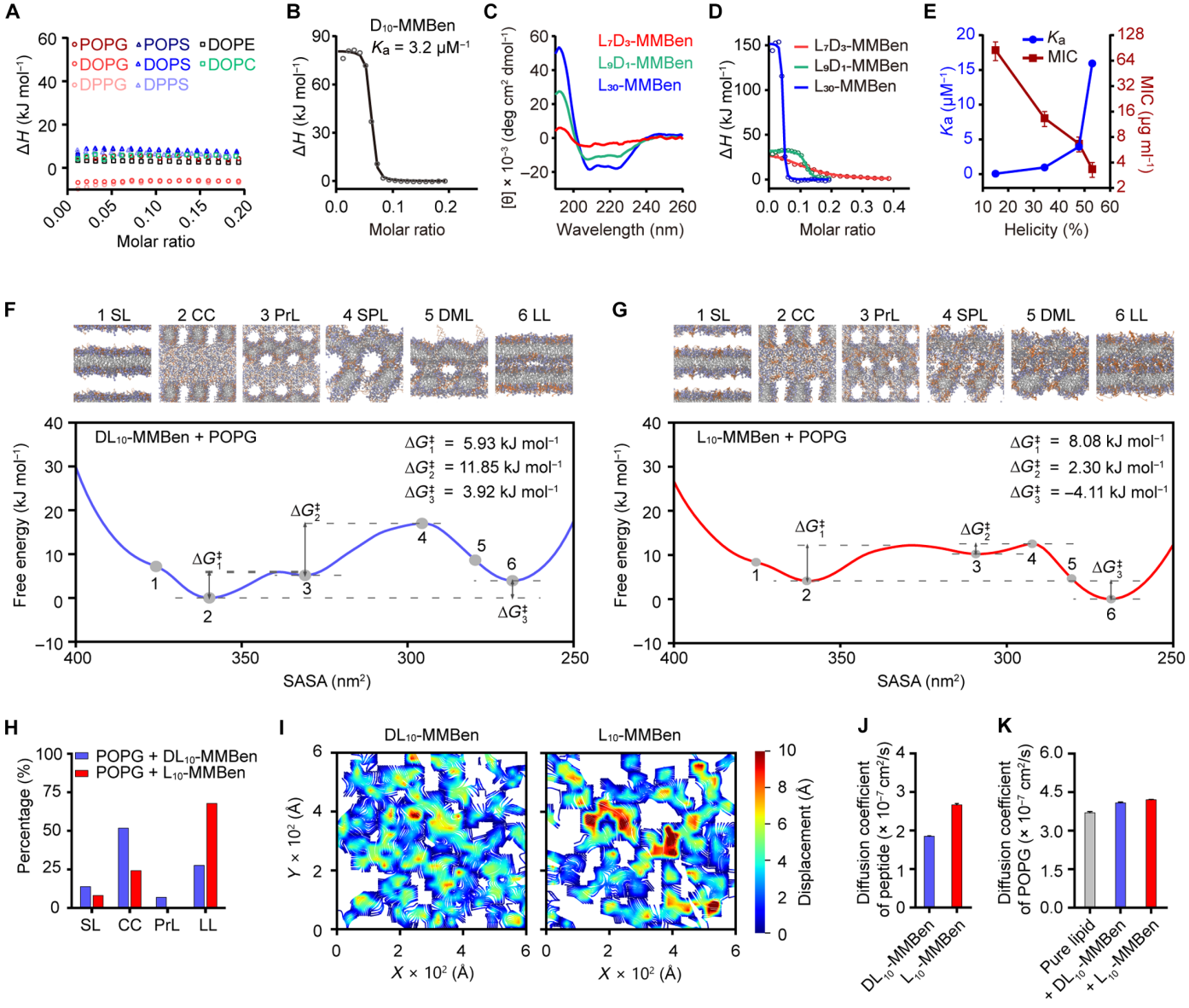

Fig. 3. Helicity is crucial for PG recognition and imparts both the thermodynamic and kinetic advantages of L_{10}-MMBen/PG assembly. (**A**) ITC-determined integrated heat release during the interaction between DL_{10}-MMBen and phospholipids. (**B**) ITC analysis and integrated heat release of the interaction between POPG and D_{10}-MMBen. (**C**) CD spectra of L_7D_3-MMBen, L_9D_1-MMBen, and L_{30}-MMBen in aqueous solution (pH 7.0). (**D**) ITC-determined integrated heat release of the interaction between POPG and peptides with different helicities. (**E**) *Ka* and minimum inhibitory concentration (MIC) values of peptides with different helicities. Data represent average values ± SD ($n = 3$ biological replicates). Free energy landscape spanned on the solvent-accessible surface area (SASA) of all peptides, and the head groups of phospholipids were derived on the basis of Markov-state-model analysis for the self-assembly of POPG phospholipids directed by DL_{10}-MMBen (**F**) or L_{10}-MMBen (**G**). Gray dots are used to guide the eye for the assembling pathways, and the representative structures during POPG self-assembly are displayed. SL, CC, PrL, SPL, DML, and LL refer to the single layer state, crossing-cylinder state, porous-rich layer state, skewed porous layer, distorted multilayer state, and layer-by-layer state, respectively. (**H**) Percentages of final state counts from assembly simulations of double-layered POPG bilayers with structured (α helix, L_{10}-MMBen) and disordered (coil, DL_{10}-MMBen) peptides. (**I**) Representative streamline visualizations for DL_{10}-MMBen and L_{10}-MMBen peptides on the surface of the POPG membrane. Diffusion coefficients of peptides (**J**) and POPG (**K**) derived by using MD simulations of peptides on the POPG membrane.

bilayer than DL_{10}-MMBen (Fig. 3, I and J). While both DL_{10}-MMBen and L_{10}-MMBen can promote POPG diffusion compared to the pure POPG bilayer, L_{10}-MMBen induces a greater enhancement of POPG diffusion (Fig. 3K). Careful inspection of the peptide distribution along the *z* axis, perpendicular to the bilayer, suggests that DL_{10}-MMBen is located closer to the interior of the POPG bilayer than L_{10}-MMBen (fig. S12C). The extended conformation facilitates the penetration of DL_{10}-MMBen deeper into the hydrophobic lipid tails (fig. S12, D and E), which may not support directing the lipids into an LL structure because the peptides work as intermediates located between the monolayers of the lipid bilayer. Our results showed that helicity enables the faster diffusion of L_{10}-MMBen in the POPG bilayer, which then facilitates the assembly of POPG phospholipids and peptides.

The hiding of hydrophobic regions is crucial for PG recognition

The α helix structure is a common feature of natural AMPs, facilitating the ordered arrangement of hydrophobic and cationic groups into a facially amphiphilic structure (Fig. 4A) (*6*). We next tested whether natural helical AMPs could also recognize PG. Nevertheless, the helical AMPs melittin and LL-37 were unable to distinguish well between PG and PS, exhibiting only a 1.1- and 1.6-fold higher affinity for POPG compared to their affinity for POPS, respectively (Fig. 4, B to E). Compared to natural AMPs, the main feature of RAPs is their radially amphiphilic structure, characterized by a hydrophobic helical core covered with cationic groups in all radial directions of the helix. We then demonstrated whether the shielding of the hydrophobic regions is crucial for the PG recognition of RAPs. We synthesized three RAPs with exposed hydrophobic tails (C6, C12, and C16) (Fig. 4F). These RAPs exhibited a stable helical structure, even under elevated temperatures and helix-destabilizing reagents (Fig. 4, G and H, and fig. S14). According to MD simulations, the alkyl tails of RAPs do not maintain a tight contact with the backbone of helical peptide, and they are flexible and can extend outward into the solution environment (fig. S15). Moreover, the alkyl tails keep fraying around the helical axis during the 50-ns MD simulations (fig. S15, C and F). As the increase of the exposed hydrophobicity, a decreased selectivity toward POPG was detected (Fig. 4I and fig. S16). On the contrary, we found that the selectivity for PG increased as hydrophobicity in the hidden hydrophobic regions of RAPs increased (Fig. 4, J to M). BuL_{10}-MMBen (fig. S17), having one more σ bond in the hiding hydrophobic domain compared

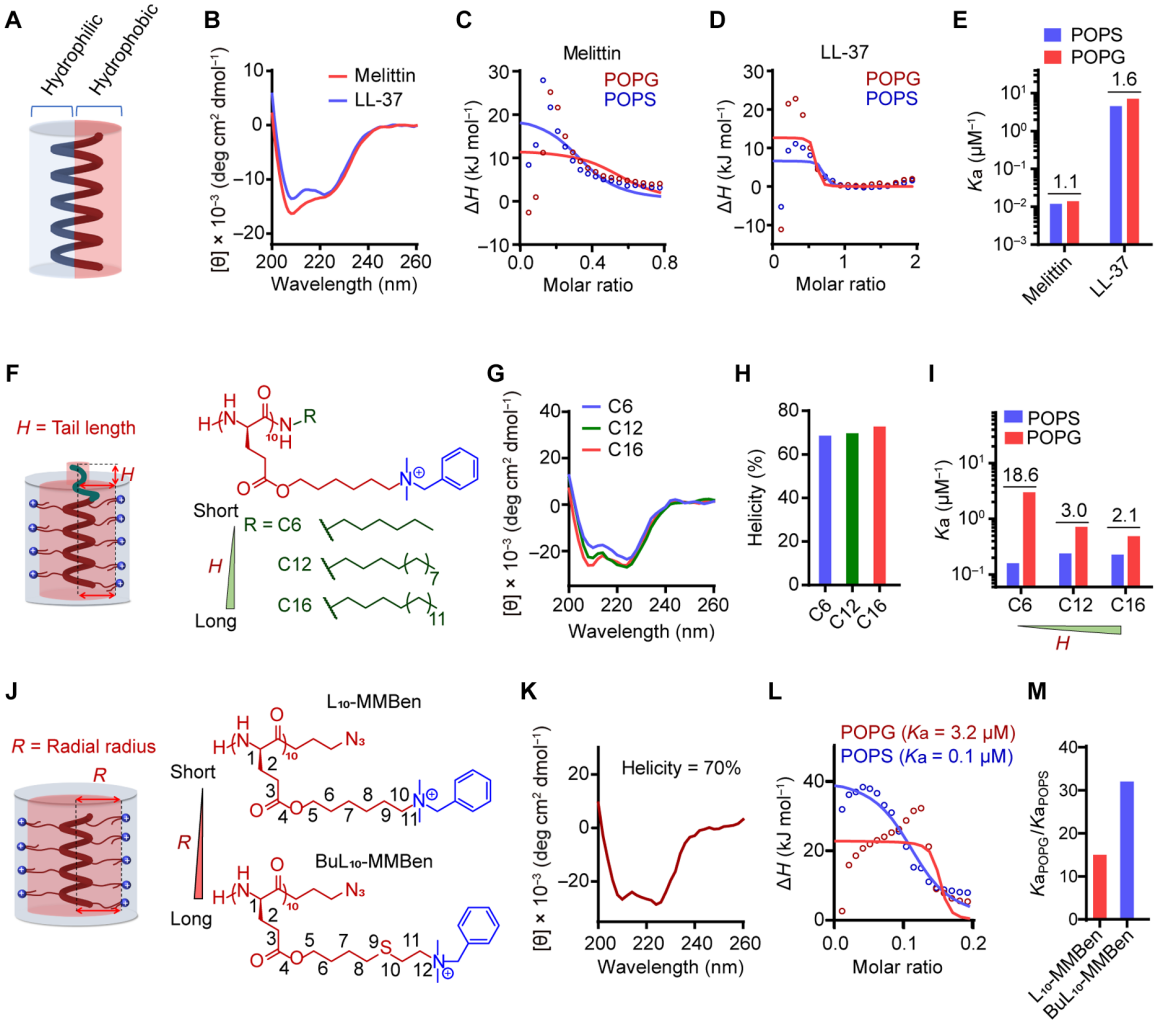

Fig. 4. The hiding of hydrophobic domain in RAPs is crucial for PG recognition. (**A**) Schematic illustration of facially amphiphilic AMPs. (**B**) CD spectra of melittin and LL-37 in PBS solution (pH 7.0). ITC-determined integrated heat release of the interaction between phospholipids and melittin (**C**) or LL-37 (**D**). (**E**) ITC-determined *Ka* between natural AMPs (melittin and LL-37) and phospholipids. (**F**) Schematic illustration of RAPs with different hydrophobic tails. CD spectra (**G**) and helicity (**H**) of RAPs with different hydrophobic tails in aqueous solution (pH 7.0). (**I**) ITC-determined *Ka* between RAPs with different hydrophobic tails and phospholipids. (**J**) Schematic illustration of RAPs with different radial radius. BuL_{10}-MMBen has one more σ bond in the hiding hydrophobic domain compared to L_{10}-MMBen. (**K**) CD spectrum of BuL_{10}-MMBen in aqueous solution (pH 7.0). (**L**) ITC-determined integrated heat release of the interaction between BuL_{10}-MMBen and phospholipids. (**M**) Multiples of the difference in *Ka* between POPG and POPS for L_{10}-MMBen and BuL_{10}-MMBen. In (E) and (I), numbers above the column charts represent multiples of the difference between Ka_{POPG} and Ka_{POPS}.

to L_{10}-MMBen, exhibited 29.7-fold higher affinity toward POPG than POPS versus 14.2-fold for L_{10}-MMBen (Fig. 4, J to M). Similar to L_{10}-MMBen, BuL_{10}-MMBen also caused the aggregation of PG-containing SUVs (fig. S18A) and induced fusion and deformation of PG-containing GUVs but not PS-containing GUVs (fig. S18, B and C). In terms of the free energy observed via CG MD simulation, the shapes of the calculated free energy landscapes for BuL_{10}-MMBen (fig. S19) and L_{10}-MMBen systems (Fig. 3G) are similar. Both of them have six discrete metastable states (SL, CC, PrL, SPL, DML, and LL) during the assembly process (fig. S19). CC and PrL are the two locally stable states besides the global minimum (LL state; fig. S19). The LL state is thermodynamically more favored compared with the metastable CC state in the BuL_{10}-MMBen system, with a ΔG of -4.67 kJ mol^{-1} (fig. S19). These observations indicate a similar mechanism for BuL_{10}-MMBen and L_{10}-MMBen when assembly with POPG lipids. These results indicated that the hiding of hydrophobic regions in RAPs is important for PG recognition.

PG recognition endows RAPs with highly selective membranolytic activity against bacteria

In comparison to the disordered DL_{10}-MMBen peptide, which has the same chemical composition, net charge, and hydrophobicity but does not recognize PG, the PG-targeting peptide L_{10}-MMBen more effectively bound to bacteria (Fig. 5A) and exhibited 1500- and 3750-fold higher antibacterial activity against *Escherichia coli* American Type Culture Collection (ATCC) 35218 (Gram-negative bacteria) and *Staphylococcus aureus* ATCC 6538 (Gram-positive bacteria), respectively (Fig. 5B). L_{10}-MMBen also exhibited much higher antibacterial activity than DL_{10}-MMBen against clinically isolated bacterial strains, including *Pseudomonas aeruginosa* (*Pae*), carbapenem-resistant *Klebsiella pneumoniae* (CRE-*Kpn*), methicillin-resistant *S. aureus* (MRSA), and extensively drug-resistant *Acinetobacter baumannii* (XDR-*Aba*) (Fig. 5C). Such big differences were inexplicable according to the typical antibacterial mechanism of AMPs through electrostatic and hydrophobic interactions. The competitive binding of L_{10}-MMBen by the addition of POPG in the medium inhibited L_{10}-MMBen from attaching to bacteria and destroying bacterial membrane (fig. S20). Moreover, preincubation with POPG significantly inhibited the antibacterial activity of L_{10}-MMBen (Fig. 5, D and E), while pretreatment with POPS produced a much lower inhibitory effect and DPPS, DOPC, and 1,2-dioleoyl-*sn*-glycero-3-phosphoethanolamine (DOPE) had not effect, confirming the specific interaction between L_{10}-MMBen and the bacterial anionic PG phospholipid (fig. S21). These results indicated that PG recognition is crucial for the antibacterial activity of L_{10}-MMBen.

Although L_{10}-MMBen and DL_{10}-MMBen showed over a 1000-fold difference in antimicrobial activity, their 10% hemolytic concentration (HC_{10}) was comparable (Fig. 5F). Consequently, L_{10}-MMBen exhibited 1500- and 3750-fold higher antibacterial selectivity [defined as HC_{10}/minimum inhibitory concentration (MIC)] against *E. coli* and *S. aureus*, respectively, compared to DL_{10}-MMBen (Fig. 5F). In a bacterial and red blood cell (RBC) coincubation system, the PG-targeting peptide L_{10}-MMBen also effectively killed bacteria while exhibiting low hemolysis against RBCs, whereas DL_{10}-MMBen showed both low bactericidal activity and low hemolytic activity (Fig. 5G). Moreover, L_{10}-MMBen effectively killed intracellular bacteria that survived within bone marrow–derived macrophages (BMDMs) (Fig. 5, H to J) and showed no obvious cytotoxicity toward BMDMs (Fig. 5K). It should be noted that L_{10}-MMO, which has minimal interaction difference between PG and PS (Fig. 1, F to H), exhibited low antibacterial selectivity, comparable to that of DL_{10}-MMO (fig. S22, A to C), while L_{10}-MMB and L_{10}-MMH, which showed an obvious interaction difference between PG and PS (especially for saturated DPPG and DPPS), exhibited over 200-fold higher antibacterial activity and selectivity against *E. coli* and *S. aureus* than corresponding DL_{10}-R peptides (fig. S22, D to F).

Next, we proved that L_{10}-MMBen killed bacteria mainly via a membranolytic mechanism and that DL_{10}-MMBen showed much lower membranolytic activity against bacteria than L_{10}-MMBen. L_{10}-MMBen caused a much greater dye leakage from bacterial cell membrane–mimicking liposomes (Fig. 5L) and induced a much higher uptake of propidium iodide, a membrane-impermeable dye, into bacterial cells than DL_{10}-MMBen (Fig. 5, M and N). Scanning electron microscopy showed that L_{10}-MMBen caused the fracture and fragmentation of bacterial membranes (Fig. 5O). TEM showed that *E. coli* cell membranes were disrupted by L_{10}-MMBen in a time-dependent manner, with inner membranes becoming distorted at 10 min and disorganized at 30 min, and whole membranes being disrupted at 60 min (Fig. 5P). By contrast, DL_{10}-MMBen treatment did not affect the *E. coli* membrane even after a 4-hour treatment (fig. S22G). A similar phenomenon was observed for L_{10}-MMBen–treated *S. aureus*, with small membrane buddings forming after 20 min of treatment and membrane disturbance occurring at 40 min (Fig. 5Q). With the membranolytic mechanism of action, L_{10}-MMBen was less prone to induce drug resistance than conventional antibiotics and did not induce resistance in *E. coli* ATCC 35218 after 40 passages of incubation (Fig. 5R), whereas after 16 passages with colistin and ciprofloxacin treatment, the MIC of corresponding drugs against *E. coli* ATCC 35218 increased by 128- and 256-fold, respectively (Fig. 5R).

The in vivo toxicity and antibacterial efficacy of L_{10}-MMBen

Helical L_{10}-MMBen and nonhelical DL_{10}-MMBen showed comparable toxicity in vivo, with maximum tolerated doses (MTDs) of 60 and 80 mg kg^{-1}, respectively, after intravenous administration into Institute of Cancer Research (ICR) mice (fig. S23A); whereas DL_{10}-MMO, which exhibited lower antimicrobial activity but higher hemolytic activity compared to L_{10}-MMBen, had an MTD of 20 mg kg^{-1} (fig. S23A). After intravenous administration at 20 mg kg^{-1}, both L_{10}-MMBen and DL_{10}-MMBen showed no significant toxicity to normal tissues according to hematoxylin and eosin staining of the heart, liver, spleen, and kidney tissues (fig. S23B) and serum biochemical indexes (Fig. 6, A and B).

Last, we evaluated the in vivo antibacterial activity of L_{10}-MMBen. In a bladder infection model, intravesical injection of DL_{10}-MMBen (70 μg per bladder) did not significantly decrease the bacterial burden in bladders, whereas L_{10}-MMBen treatment reduced the bacterial burden by 2.7- and 16.0-fold at doses of 35 and 70 μg per bladder, respectively (Fig. 6, C and D). L_{10}-MMBen could also benefit in a CLP-induced severe sepsis model, which is the gold standard model for polymicrobial sepsis and shares similar characteristics of the progression and characteristics of human sepsis (*45*, *46*). L_{10}-MMBen (2 mg kg^{-1}) treatment significantly increased the survival rate of CLP-induced mice to 79.0% within 80 hours, compared to only 30.8% survival in the phosphate-buffered saline (PBS) treatment group (Fig. 6, E and F). In contrast, DL_{10}-MMBen (2 mg kg^{-1}) treatment showed no significant improvement (Fig. 6, E and F).

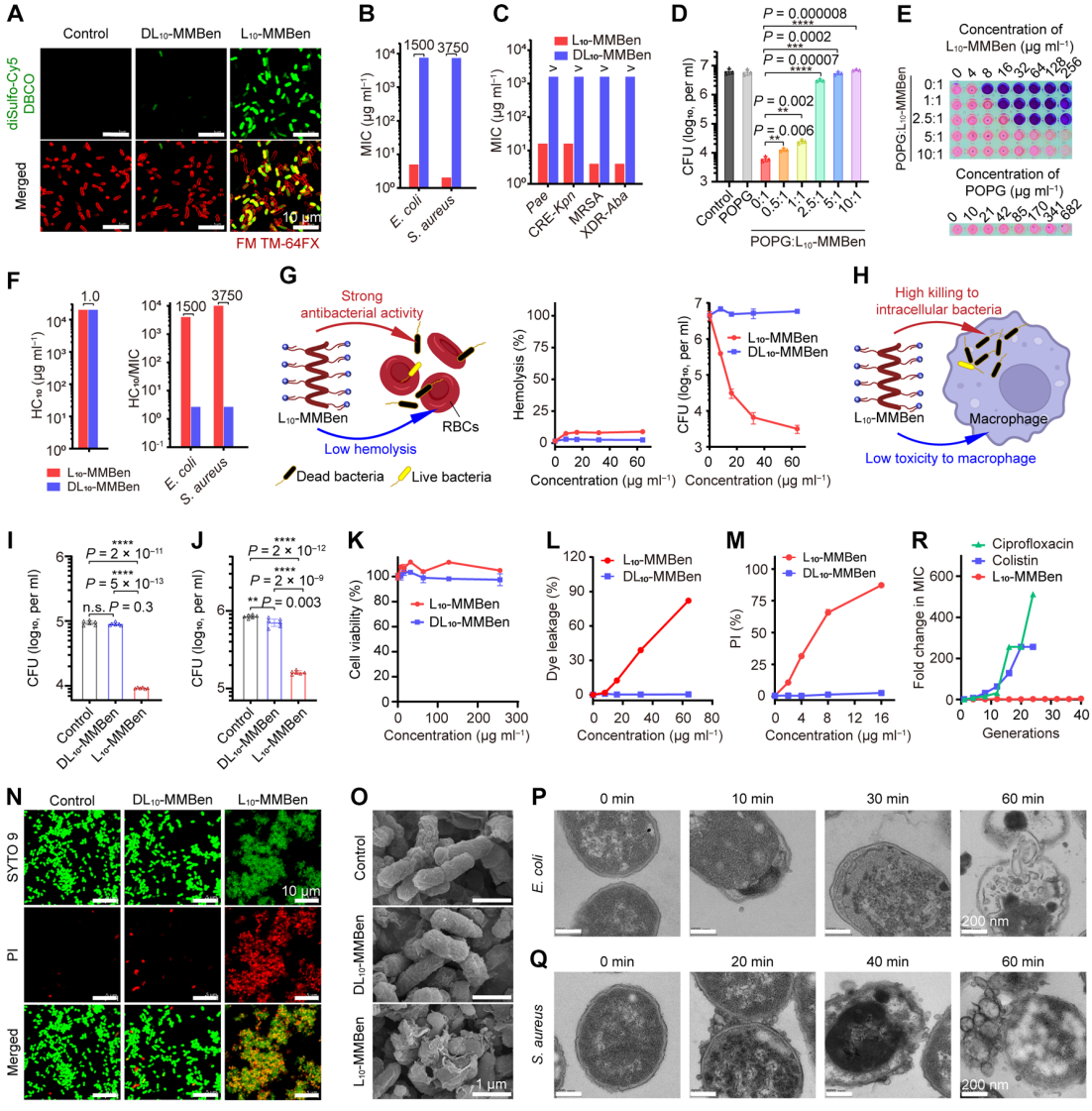

Fig. 5. PG recognition endows L_{10}-MMBen with highly selective membranolytic activity against bacteria. (**A**) Confocal images of *E. coli* American Type Culture Collection (ATCC) 35218 treated with L_{10}-MMBen or DL_{10}-MMBen (250 μg ml^{-1}) for 60 min. Scale bars, 10 μm. Bacterial membranes were stained with FM™ 4-64FX (red), and DL_{10}-MMBen and L_{10}-MMBen were stained with diSulfo-Cy5 dibenzocyclooctyne (DBCO) (green). (**B**) MIC values of L_{10}-MMBen and DL_{10}-MMBen against *E. coli* ATCC 35218 and *S. aureus* ATCC 6538. (**C**) MIC values of L_{10}-MMBen and DL_{10}-MMBen against clinically isolated bacteria, including *P. aeruginosa* (*Pae*), carbapenem-resistant *K. pneumoniae* (CRE-*Kpn*), methicillin-resistant *S. aureus* (MRSA), and extensively drug-resistant *A. baumannii* (XDR-*Aba*). > represents an MIC value higher than 1028 μg ml^{-1}. (**D**) Colony-forming units (CFU) of *E. coli* ATCC 35218 after 4 hours of incubation with L_{10}-MMBen (32 μg ml^{-1}) when preincubated with different molar ratios of POPG. Bacterial suspensions incubated with medium only (control) or POPG (85 μg ml^{-1}) were used as negative controls. (**E**) The antibacterial activity of L_{10}-MMBen when preincubated with different molar ratios of POPG as detected by the resazurin blue assay. Pink indicates bacterial growth, whereas blue indicates no bacterial growth. (**F**) HC_{10} and selectivity index (HC_{10}/MIC) of L_{10}-MMBen and DL_{10}-MMBen. HC_{10} refers to the concentration at which the peptide causes 10% hemolysis against red blood cells (RBCs). (**G**) Schematic illustration of the selective bacteria killing of L_{10}-MMBen in bacteria (*E. coli* ATCC 35218) and RBC coincubation solution (left). The hemolysis ratio (middle) and viable bacteria numbers in CFU (right) were determined after 4 hours of incubation with various concentrations of L_{10}-MMBen or DL_{10}-MMBen. (**H**) Schematic illustration of the selective bacteria killing of L_{10}-MMBen toward intracellular bacteria in macrophages. CFU of *E. coli* ATCC 35218 (**I**) and *S. aureus* ATCC 6538 (**J**) survived in bone marrow–derived macrophage (BMDM) cells after treatment with L_{10}-MMBen or DL_{10}-MMBen (128 μg ml^{-1}) for 12 hours. n.s., not significant. (**K**) Cell viability of BMDM cells when incubated with L_{10}-MMBen or DL_{10}-MMBen at different concentrations for 12 hours. (**L**) Dye leakage from bacterial cell membrane–mimicking liposomes when incubated with L_{10}-MMBen or DL_{10}-MMBen at various concentrations for 5 min. (**M**) Flow cytometry analysis of propidium iodide (PI) uptake after incubation with L_{10}-MMBen or DL_{10}-MMBen at various concentrations. (**N**) Live/dead (SYTO 9/PI) staining of *E. coli* ATCC 35218 treated with L_{10}-MMBen or DL_{10}-MMBen (128 μg ml^{-1}) for 4 hours. SYTO 9, green; PI, red. Scale bars, 10 μm. (**O**) Scanning electron microscopy (SEM) images of *E. coli* ATCC 35218 treated with L_{10}-MMBen or DL_{10}-MMBen (128 μg ml^{-1}) for 4 hours. Scale bars, 1 μm. TEM images of *E. coli* ATCC 35218 (**P**) and *S. aureus* ATCC 6538 (**Q**) treated with L_{10}-MMBen (128 μg ml^{-1}) for different time intervals. Scale bars, 200 nm. (**R**) Fold change in MIC values of antimicrobials against *E. coli* ATCC 35218 during serial passaging in sub-MIC concentrations of antimicrobials. In (B) and (F), numbers above the column charts represent multiples of the difference in MIC, HC_{10}, and selectivity index between L_{10}-MMBen and DL_{10}-MMBen. In (D), (G), and (I) to (M), data represent average values ± SD [$n = 3$ biological replicates for (D), (G), and (K) to (M); $n = 6$ biological replicates for (I) and (J)]. Statistical significance was determined by unpaired two-tailed Student's *t* test. In (A) and (N), representative confocal images from two independent samples are shown. In (O) to (Q), representative SEM and TEM images are shown (at least three images were taken for each sample).

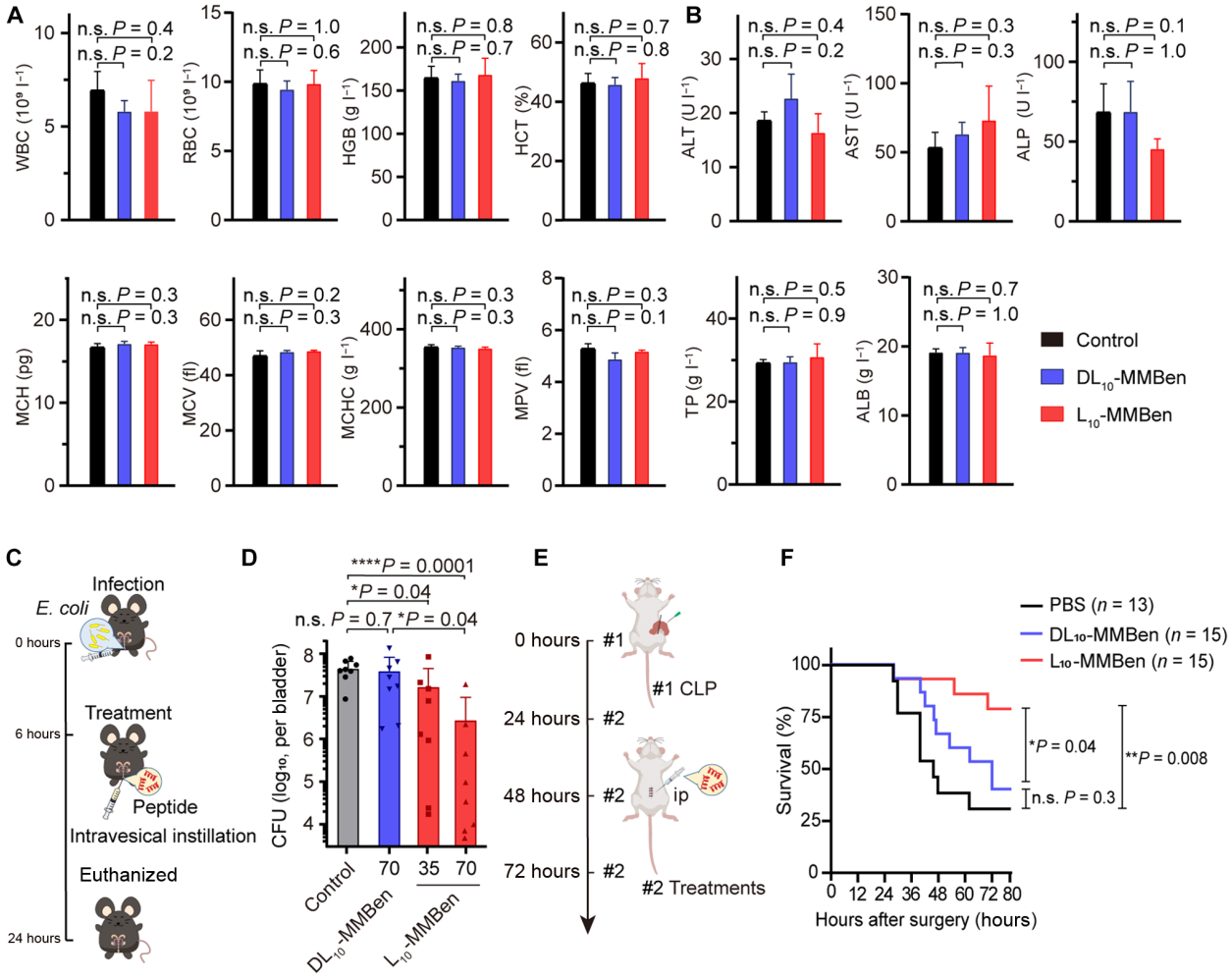

Fig. 6. The in vivo toxicity and antibacterial efficacy of L_{10}-MMBen. Routine blood tests (**A**) and blood biochemical tests (**B**) of mice ($n = 3$ per group) treated with one dose of PBS, DL_{10}-MMBen, or L_{10}-MMBen (20 mg kg^{-1}). WBC, white blood cell count; RBC, red blood cell count; HGB, hemoglobin; HCT, hematocrit; MCH, mean corpuscular hemoglobin; MCV, mean corpuscular volume; MCHC, mean corpuscular hemoglobin concentration; MPV, mean platelet volume; ALT, alanine aminotransferase; AST, aspartate aminotransferase; ALP, alkaline phosphatase; TP, total protein; ALB, albumin. (**C**) Schematic of the construction and treatment schedule of the bladder infection model ($n = 8$ per group). Mice were treated with peptides via intravesical instillation 6 hours after infection and were euthanized 24 hours after infection for the detection of bacterial burden in bladders. (**D**) Bacterial burden in bladders after treatment with PBS, DL_{10}-MMBen (70 μg per bladder), or L_{10}-MMBen (35 or 70 μg per bladder). (**E**) Schematic of the construction and treatment schedule of the CLP-induced severe sepsis model. PBS, DL_{10}-MMBen, or L_{10}-MMBen [2 mg kg^{-1}, intraperitoneally (ip)] was administered at 24, 48, and 72 hours after CLP. (**F**) Survival of the infected mice after treatment with PBS ($n = 13$), DL_{10}-MMBen ($n = 15$), or L_{10}-MMBen ($n = 15$). In (A), (B), and (D), data represent average values ± SEM, and the statistical significance was determined with an unpaired two-tailed Student's *t* test. In (F), the statistical significance was determined with Kaplan-Meier survival analysis.

DISCUSSION

Our study presents a design of highly selective AMPs via incorporating a paradigm of specific bacterial phospholipid recognition. PG targeting can be set as a design rule for AMPs, providing an additional dimension to enhance their antibacterial selectivity and reduce their toxicity to mammalian cells. The development of bacterial phospholipid-targeting peptides could enable broad applications in the design of antimicrobials, bacteria-targeting drug delivery systems, and diagnostic tools for bacterial infection.

We revealed the crucial role of α helix structure in the recognition of bacterial phospholipid PG, offering an insight into the understanding of the secondary structure of AMPs. The α helix structure has been demonstrated to be positively correlated with both the antimicrobial activity and toxicity of AMPs. However, the contribution of the α helix structure to the selectivity of AMPs is controversial and context dependent (*47*–*50*). Typically, the α helix structure of facially amphiphilic AMPs results in the aggregation of hydrophobic residues and an increase in unspecific hydrophobic driving force for binding to both bacterial and mammalian cell membranes. In this study, we proved that the hiding of hydrophobic regions is crucial for PG recognition of RAPs. Correspondingly, our study demonstrated that PG recognition was limited for L_{10}-MMO and C16-L_{10}-MMBen with highly hydrophobic side chains and terminal group, respectively. In line with the concealed hydrophobic region, the helical structure of L_{10}-MMBen did not promote the insertion into cell membranes but directed the rearrangement of

PG. Our finding provides valuable insights into the function of the helical structure in AMPs, offering a perspective for the design and development of AMPs with high bacterial selectivity.

RAPs exhibit advantages including selective recognition of PG over PS and reduced likelihood of inducing resistance compared to conventional antibiotics. However, RAPs synthesized through NCA polymerization exhibit polydispersity. The polydispersity could affect the helicity of RAPs and the *Ka* between RAPs and phospholipids. Developing RAPs with a precise structure is important for advancing their applications further.

MATERIALS AND METHODS

Lipids

POPG, DPPG, DOPG, POPC, DOPC, 1,2-dipalmitoyl-*rac*-glycero-3-phosphocholine, DOPE, and DPPS were obtained from Inc. AVT (Shanghai) Pharmaceutical Tech Co. Ltd. POPS and DOPS were purchased from Anatrace Products LLC (USA). DLPG was purchased from Sigma-Aldrich (USA). SM (milk, bovine), NBD-PG, and NBD-PC were purchased from Avanti Polar Lipids (USA). CL was purchased from Aladdin (China).

Cells

Standard bacterial strains of *E. coli* ATCC 35218 and *S. aureus* ATCC 6538 were sourced from ATCC. All clinically isolated strains, including *Pae* (190836), CRE-*Kpn* (190949), MRSA (190809), and XDR-*Aba* (181442), were provided by S. Huang from Sun Yat-Sen Memorial Hospital, Sun Yat-Sen University. All bacterial strains were cultured in LB medium [tryptones (10 g liter^{-1}), NaCl (10 g liter^{-1}), and yeast extract (5 g liter^{-1}) in 1 liter of H_2O] overnight at 37°C with shaking (220 rpm). Unless otherwise stated, M9 medium [sodium phosphate buffer (6.8 g liter^{-1}), KH_2PO_4 (3 g liter^{-1}), NaCl (0.5 g liter^{-1}), NH_4Cl (1 g liter^{-1}), glucose (4 g liter^{-1}), $MgSO_4$ (0.24 g liter^{-1}), and $CaCl_2$ (0.011 g liter^{-1})] was used for antimicrobial tests. BMDMs were obtained according to the literature and maintained in tissue culture flasks in Dulbecco's modified Eagle's medium containing 10% fetal bovine serum (*51*).

Synthesis of RAPs

Chlorine-functionalized peptides (PCHXG$_n$, X = L, D, DL, L_7D_3, or L_9D_1, where *n* refers to the DP) were synthesized according to our previous work (*16*, *17*) by using anhydrous 3-azido-1-propanamine (N_3), hexylamine (C6), lauryl amine (C12), and cetylamine (C16) as the initiators. PCHXG$_n$ (100 mg, 0.4 mmol of Cl groups) and NaI (0.3 g, 2 mmol) were dissolved in *N*,*N*-dimethylformamide (2 ml) and acetonitrile (2 ml), and then tertiary amine (MMO, MMH, MMB, or MMBen) (2 mmol) was added. The mixture was stirred at 80°C for 48 hours. After most of the solvent was removed under vacuum, NaCl (1.0 M, 3 ml) was added. The solution was then stirred at room temperature for 3 hours to promote ion exchange. The product was purified by dialysis (molecular weight cutoff = 1 kDa) against distilled water for 3 days. A white solid powder was obtained after lyophilization. BuL_{10}-MMBen was synthesized according to our previous work through NCA polymerization and thiol-ene reactions (*52*).

ITC detection

ITC was used to assess the interaction between peptides and lipids. Peptide solutions (1.25 mM in PBS) were loaded into the ITC syringe. Phospholipids (0.25 to 1.25 mM in PBS) were loaded into the ITC cell. Thermograms were recorded at 25°C with stirring at 750 rpm and at a reference power of 10 μcal s^{-1}. Nineteen injections of 36.4 μl were performed separated by 150 s with 60 s of initial delay. ITC assays were measured on a MicroCal PEAQ-ITC system (Malvern Panalytical Technologies Corporation, UK). Data were analyzed in MicroCal PEAQ-ITC Analysis Software 1.1.0.1262.

Animals

Female C57BL/6 mice (7 to 8 weeks) and female ICR mice (5 to 6 weeks) were purchased from Guangdong Sijiajingda Biotechnology Co. Ltd. (China). Mice were maintained in a standardized environmental condition (temperature, 23 ± 2°C; humidity, 55 ± 10%). Mice received care in strict accordance with the regulations for the Administration of Affairs Concerning Experimental Animals approved by the State Council of People's Republic of China. The CLP-induced sepsis model and toxicity test were approved by the Animal Research Ethics Sub-Committee of South China University of Technology (number for approval: 2023037). The bladder infection model was approved by the Animal Research Ethics Sub-Committee of University of Science and Technology of China (number for approval: USTCACUC24020123081).

Mouse infection models

For the mouse bladder infection model, C57BL/6 female mice (n = 8 per group) were infected with a dose of 5.0×10^7 colony-forming units per bladder *E. coli* ATCC35218 suspension via intravesical instillation. Mice were treated 6 hours after infection with PBS, L_{10}-MMBen (35 or 70 μg per bladder) or DL_{10}-MMBen (70 μg per bladder) via intravesical instillation. Mice were euthanized 24 hours after infection. Bladders were removed, homogenized in sterile PBS, serially diluted, and plated on LB agar for bacterial colony counting. The CLP-induced sepsis model was developed in ICR female mice according to the literature (*46*). PBS, DL_{10}-MMBen [2 mg kg^{-1}, intraperitoneally (ip)], or L_{10}-MMBen (2 mg kg^{-1}, ip) was administered at 24, 48, and 72 hours after CLP. Survival of the infected mice was observed after the treatments.

Statistical analysis

Data are expressed as the means ± SD for in vitro studies and as the means ± SEM for animal experiments. Differences between groups were assessed using GraphPad Prism 8.0.2, with unpaired two-tailed Student's *t* tests for the calculation of *P* values. Statistical significance was set at $^*P < 0.05$, $^{**}P < 0.01$, $^{***}P < 0.001$, and $^{****}P < 0.0001$.

Supplementary Materials

This PDF file includes:

Supplementary Text
Schemes S1 to S3
Figs. S1 to S24
Tables S1 to S7
References

REFERENCES AND NOTES

1. L. Liu, K. Xu, H. Wang, P. K. Jeremy Tan, W. Fan, S. S. Venkatraman, L. Li, Y.-Y. Yang, Self-assembled cationic peptide nanoparticles as an efficient antimicrobial agent. *Nat. Nanotechnol.* **4**, 457–463 (2009).
2. F. Nederberg, Y. Zhang, J. P. K. Tan, K. Xu, H. Wang, C. Yang, S. Gao, X. D. Guo, K. Fukushima, L. Li, J. L. Hedrick, Y.-Y. Yang, Biodegradable nanostructures with selective lysis of microbial membranes. *Nat. Chem.* **3**, 409–414 (2011).

3. V. Lázár, A. Martins, R. Spohn, L. Daruka, G. Grézal, G. Fekete, M. Számel, P. K. Jangir, B. Kintses, B. Csörgő, Á. Nyerges, Á. Györkei, A. Kincses, A. Dér, F. R. Walter, M. A. Deli, E. Urbán, Z. Hegedűs, G. Olajos, O. Méhi, B. Bálint, I. Nagy, T. A. Martinek, B. Papp, C. Pál, Antibiotic-resistant bacteria show widespread collateral sensitivity to antimicrobial peptides. *Nat. Microbiol.* **3**, 718–731 (2018).
4. R. Spohn, L. Daruka, V. Lázár, A. Martins, F. Vidovics, G. Grézal, O. Méhi, B. Kintses, M. Számel, P. K. Jangir, B. Csörgő, Á. Györkei, Z. Bódi, A. Faragó, L. Bodai, I. Földesi, D. Kata, G. Maróti, B. Pap, R. Wirth, B. Papp, C. Pál, Integrated evolutionary analysis reveals antimicrobial peptides with limited resistance. *Nat. Commun.* **10**, 4538 (2019).
5. A. L. Hilchie, K. Wuerth, R. E. Hancock, Immune modulation by multifaceted cationic host defense (antimicrobial) peptides. *Nat. Chem. Biol.* **9**, 761–768 (2013).
6. S. Bobone, L. Stella, Selectivity of antimicrobial peptides: A complex interplay of multiple equilibria. *Adv. Exp. Med. Biol.* **1117**, 175–214 (2019).
7. E. F. Palermo, K. Lienkamp, E. R. Gillies, P. J. Ragogna, Antibacterial activity of polymers: Discussions on the nature of amphiphilic balance. *Angew. Chem. Int. Ed.* **58**, 3690–3693 (2019).
8. A. G. Elliott, J. X. Huang, S. Neve, J. Zuegg, I. A. Edwards, A. K. Cain, C. J. Boinett, L. Barquist, C. V. Lundberg, J. Steen, M. S. Butler, M. Mobli, K. M. Porter, M. A. T. Blaskovich, S. Lociuro, M. Strandh, M. A. Cooper, An amphipathic peptide with antibiotic activity against multidrug-resistant Gram-negative bacteria. *Nat. Commun.* **11**, 3184 (2020).
9. J. Xie, M. Zhou, Y. Qian, Z. Cong, S. Chen, W. Zhang, W. Jiang, C. Dai, N. Shao, Z. Ji, J. Zou, X. Xiao, L. Liu, M. Chen, J. Li, R. Liu, Addressing MRSA infection and antibacterial resistance with peptoid polymers. *Nat. Commun.* **12**, 5898 (2021).
10. J. Huang, Y. Xu, Y. Xue, Y. Huang, X. Li, X. Chen, Y. Xu, D. Zhang, P. Zhang, J. Zhao, J. Ji, Identification of potent antimicrobial peptides via a machine-learning pipeline that mines the entire space of peptide sequences. *Nat. Biomed. Eng.* **7**, 797–810 (2023).
11. M. Song, Y. Liu, X. Huang, S. Ding, Y. Wang, J. Shen, K. Zhu, A broad-spectrum antibiotic adjuvant reverses multidrug-resistant Gram-negative pathogens. *Nat. Microbiol.* **5**, 1040–1050 (2020).
12. L. Liu, K. C. Courtney, S. W. Huth, L. A. Rank, B. Weisblum, E. R. Chapman, S. H. Gellman, Beyond amphiphilic balance: Changing subunit stereochemistry alters the pore-forming activity of nylon-3 polymers. *J. Am. Chem. Soc.* **143**, 3219–3230 (2021).
13. Y. Qian, S. Deng, Z. Cong, H. Zhang, Z. Lu, N. Shao, S. A. Bhatti, C. Zhou, J. Cheng, S. H. Gellman, R. Liu, Secondary amine pendant β-peptide polymers displaying potent antibacterial activity and promising therapeutic potential in treating MRSA-induced wound infections and keratitis. *J. Am. Chem. Soc.* **144**, 1690–1699 (2022).
14. J. Tan, J. Tay, J. Hedrick, Y. Y. Yang, Synthetic macromolecules as therapeutics that overcome resistance in cancer and microbial infection. *Biomaterials* **252**, 120078 (2020).
15. Y. Shi, G. Yin, Z. Yan, P. Sang, M. Wang, R. Brzozowski, P. Eswara, L. Wojtas, Y. Zheng, X. Li, J. Cai, Helical sulfono-γ-AApeptides with aggregation-induced emission and circularly polarized luminescence. *J. Am. Chem. Soc.* **141**, 12697–12706 (2019).
16. M. Xiong, M. W. Lee, R. A. Mansbach, Z. Song, Y. Bao, R. M. Peek Jr., C. Yao, L.-F. Chen, A. L. Ferguson, G. C. L. Wong, J. Cheng, Helical antimicrobial polypeptides with radial amphiphilicity. *Proc. Natl. Acad. Sci. U.S.A.* **112**, 13155–13160 (2015).
17. M. Xiong, Y. Bao, X. Xu, H. Wang, Z. Han, Z. Wang, Y. Liu, S. Huang, Z. Song, J. Chen, R. M. Peek Jr., L. Yin, L.-F. Chen, J. Cheng, Selective killing of *Helicobacter pylori* with pH-responsive helix-coil conformation transitionable antimicrobial polypeptides. *Proc. Natl. Acad. Sci. U.S.A.* **114**, 12675–12680 (2017).
18. H. Zhang, Q. Chen, J. Xie, Z. Cong, C. Cao, W. Zhang, D. Zhang, S. Chen, J. Gu, S. Deng, Z. Qiao, X. Zhang, M. Li, Z. Lu, R. Liu, Switching from membrane disrupting to membrane crossing, an effective strategy in designing antibacterial polypeptide. *Sci. Adv.* **9**, eabn0771 (2023).
19. K. D. Roberts, Y. Zhu, M. A. K. Azad, M.-L. Han, J. Wang, L. Wang, H. H. Yu, A. S. Horne, J.-A. Pinson, D. Rudd, N. H. Voelcker, N. A. Patil, J. Zhao, X. Jiang, J. Lu, K. Chen, O. Lomovskaya, S. J. Hecker, P. E. Thompson, R. L. Nation, M. N. Dudley, D. C. Griffith, T. Velkov, J. Li, A synthetic lipopeptide targeting top-priority multidrug-resistant Gram-negative pathogens. *Nat. Commun.* **13**, 1625 (2022).
20. N. Mookherjee, M. A. Anderson, H. P. Haagsman, D. J. Davidson, Antimicrobial host defence peptides: Functions and clinical potential. *Nat. Rev. Drug Discov.* **19**, 311–332 (2020).
21. C. D. Fjell, J. A. Hiss, R. E. Hancock, G. Schneider, Designing antimicrobial peptides: Form follows function. *Nat. Rev. Drug Discov.* **11**, 37–51 (2011).
22. R. E. W. Hancock, Cationic antimicrobial peptides: Towards clinical applications. *Expert Opin. Investig. Drugs* **9**, 1723–1729 (2000).
23. Y. M. Zhang, C. O. Rock, Membrane lipid homeostasis in bacteria. *Nat. Rev. Microbiol.* **6**, 222–233 (2008).
24. M. A. Rahman, M. Bam, E. Luat, M. S. Jui, M. S. Ganewatta, T. Shokfai, M. Nagarkatti, A. W. Decho, C. Tang, Macromolecular-clustered facial amphiphilic antimicrobials. *Nat. Commun.* **9**, 5231 (2018).
25. S. J. Lam, N. M. O'Brien-Simpson, N. Pantarat, A. Sulistio, E. H. H. Wong, Y.-Y. Chen, J. C. Lenzo, J. A. Holden, A. Blencowe, E. C. Reynolds, G. G. Qiao, Combating multidrug-resistant Gram-negative bacteria with structurally nanoengineered antimicrobial peptide polymers. *Nat. Microbiol.* **1**, 16162 (2016).
26. A. C. Engler, N. Wiradharma, Z. Y. Ong, D. J. Coady, J. L. Hedrick, Y.-Y. Yang, Emerging trends in macromolecular antimicrobials to fight multi-drug-resistant infections. *Nano Today* **7**, 201–222 (2012).
27. B. P. Mowery, A. H. Lindner, B. Weisblum, S. S. Stahl, S. H. Gellman, Structure-activity relationships among random nylon-3 copolymers that mimic antibacterial host-defense peptides. *J. Am. Chem. Soc.* **131**, 9735–9745 (2009).
28. R. Liu, X. Chen, S. P. Falk, B. P. Mowery, A. J. Karlsson, B. Weisblum, S. P. Palecek, K. S. Masters, S. H. Gellman, Structure-activity relationships among antifungal nylon-3 polymers: Identification of materials active against drug-resistant strains of candida albicans. *J. Am. Chem. Soc.* **136**, 4333–4342 (2014).
29. Z. Fang, J. Chen, Y. Zhu, G. Hu, H. Xin, K. Guo, Q. Li, L. Xie, L. Wang, X. Shi, Y. Wang, C. Mao, High-throughput screening and rational design of biofunctionalized surfaces with optimized biocompatibility and antimicrobial activity. *Nat. Commun.* **12**, 3757 (2021).
30. J. G. Kay, G. D. Fairn, Distribution, dynamics and functional roles of phosphatidylserine within the cell. *Cell Commun. Signal* **17**, 126 (2019).
31. T. Harayama, H. Riezman, Understanding the diversity of membrane lipid composition. *Nat. Rev. Mol. Cell Biol.* **19**, 281–296 (2018).
32. H. Strahl, J. Errington, Bacterial membranes: Structure, domains, and function. *Annu. Rev. Microbiol.* **71**, 519–538 (2017).
33. K. L. F. Hilton, C. Manwani, J. E. Boles, L. J. White, S. Ozturk, M. D. Garrett, J. R. Hiscock, The phospholipid membrane compositions of bacterial cells, cancer cell lines and biological samples from cancer patients. *Chem. Sci.* **12**, 13273–13282 (2021).
34. E. A. Bishop, M. A. C. Bermingham, Lipid composition of Gram-negative bacteria, sensitive and resistant to streptomycin. *Antimicrob. Agents Chemother.* **4**, 378–379 (1973).
35. H. Lu, J. Wang, Y. Bai, J. W. Lang, S. Liu, Y. Lin, J. Cheng, Ionic polypeptides with unusual helical stability. *Nat. Commun.* **2**, 206 (2011).
36. D. H. de Jong, G. Singh, W. F. Drew Bennett, C. Arnarez, T. A. Wassenaar, L. V. Schäfer, X. Periole, D. P. Tieleman, S. J. Marrink, Improved parameters for the martini coarse-grained protein force field. *J. Chem. Theor. Comput.* **9**, 687–697 (2013).
37. S. J. Marrink, H. J. Risselada, S. Yefimov, D. P. Tieleman, A. H. de Vries, The MARTINI force field: Coarse grained model for biomolecular simulations. *J. Phys. Chem. B* **111**, 7812–7824 (2007).
38. A. Tuerkova, I. Kabelka, T. Králová, L. Sukeník, Š. Pokorná, M. Hof, R. Vácha, Effect of helical kink in antimicrobial peptides on membrane pore formation. *eLife* **9**, e47946 (2020).
39. M. Nguyen, J. L. Stigliani, G. Pratviel, C. Bonduelle, Nucleopolypeptides with DNA-triggered α helix-to-β sheet transition. *Chem. Commun.* **53**, 7501–7504 (2017).
40. C. Bonduelle, Secondary structures of synthetic polypeptide polymers. *Polym. Chem.* **9**, 1517–1529 (2018).
41. Y. Li, Z. Qian, L. Ma, S. Hu, D. Nong, C. Xu, F. Ye, Y. Lu, G. Wei, M. Li, Single-molecule visualization of dynamic transitions of pore-forming peptides among multiple transmembrane positions. *Nat. Commun.* **7**, 12906 (2016).
42. V. S. Pande, K. Beauchamp, G. R. Bowman, Everything you wanted to know about Markov State Models but were afraid to ask. *Methods* **52**, 99–105 (2010).
43. B. E. Husic, V. S. Pande, Markov state models: From an art to a science. *J. Am. Chem. Soc.* **140**, 2386–2396 (2018).
44. S. Munro, Lipid rafts: Elusive or illusive? *Cell* **115**, 377–388 (2003).
45. D. Rittirsch, M. S. Huber-Lang, M. A. Flierl, P. A. Ward, Immunodesign of experimental sepsis by cecal ligation and puncture. *Nat. Protoc.* **4**, 31–36 (2009).
46. J. Dawulieti, M. Sun, Y. Zhao, D. Shao, H. Yan, Y.-H. Lao, H. Hu, L. Cui, X. Lv, F. Liu, C.-W. Chi, Y. Zhang, M. Li, M. Zhang, H. Tian, X. Chen, K. W. Leong, L. Chen, Treatment of severe sepsis with nanoparticulate cell-free DNA scavengers. *Sci. Adv.* **6**, eaay7148 (2020).
47. Y. B. Huang, J. F. Huang, Y. X. Chen, Alpha-helical cationic antimicrobial peptides: Relationships of structure and function. *Protein Cell* **1**, 143–152 (2010).
48. M. Dathe, M. Schümann, T. Wieprecht, A. Winkler, M. Beyermann, E. Krause, K. Matsuzaki, O. Murase, M. Bienert, Peptide helicity and membrane surface charge modulate the balance of electrostatic and hydrophobic interactions with lipid bilayers and biological membranes. *Biochemistry* **35**, 12612–12622 (1996).
49. Y. B. Liang, X. S. Zhang, Y. L. Yuan, Y. Bao, M. H. Xiong, Role and modulation of the secondary structure of antimicrobial peptides to improve selectivity. *Biomater. Sci.* **8**, 6858–6866 (2020).
50. Y. Huang, L. He, G. Li, N. Zhai, H. Jiang, Y. Chen, Role of helicity of α-helical antimicrobial peptides to improve specificity. *Protein Cell* **5**, 631–642 (2014).
51. J. I. Jun, L. F. Lau, CCN1 is an opsonin for bacterial clearance and a direct activator of Toll-like receptor signaling. *Nat. Commun.* **11**, 1242 (2020).
52. X. Hu, J. Li, Y. Zhang, M. Xiong, H. B. Zhang, Y. Yuan, A helical oncolytic polypeptide with potent membranolytic activity for cancer therapy. *Biomater. Sci.* **11**, 1451–1458 (2023).
53. J. Liu, S. Xiao, J. Li, B. Yuan, K. Yang, Y. Ma, Molecular details on the intermediate states of melittin action on a cell membrane. *BBA-Biomembranes* **1860**, 2234–2241 (2018).
54. C. Xu, W. Ma, K. Wang, K. He, Z. Chen, J. Liu, K. Yang, B. Yuan, Correlation between single-molecule dynamics and biological functions of antimicrobial peptide melittin. *J. Phys. Chem. Lett.* **11**, 4834–4841 (2020).

55. X. Periole, S. J. Marrink, The Martini coarse-grained force field. *Methods Mol. Biol.* **924**, 533–565 (2013).
56. X. Periole, M. Cavalli, S.-J. Marrink, M. A. Ceruso, Combining an elastic network with a coarse-grained molecular force field: Structure, dynamics, and intermolecular recognition. *J. Chem. Theory Comput.* **5**, 2531–2543 (2009).
57. Y. Qi, H. I. Ingólfsson, X. Cheng, J. Lee, S. J. Marrink, W. Im, CHARMM-GUI Martini maker for coarse-grained simulations with the Martini force field. *J. Chem. Theory Comput.* **11**, 4486–4494 (2015).
58. R. Fletcher, M. J. Powell, A rapidly convergent descent method for minimization. *Comput. J.* **6**, 163–168 (1963).
59. D. Van Der Spoel, E. Lindahl, B. Hess, G. Groenhof, A. E. Mark, H. J. C. Berendsen, GROMACS: Fast, flexible, and free. *J. Comput. Chem.* **26**, 1701–1718 (2005).
60. A. P. Thompson, S. J. Plimpton, W. Mattson, General formulation of pressure and stress tensor for arbitrary many-body interaction potentials under periodic boundary conditions. *J. Chem. Phys.* **131**, 154107 (2009).
61. G. Bussi, D. Donadio, M. Parrinello, Canonical sampling through velocity rescaling. *J. Chem. Phys.* **126**, 014101 (2007).
62. M. Parrinello, A. Rahman, Strain fluctuations and elastic constants. *J. Chem. Phys.* **76**, 2662–2666 (1982).
63. W. Humphrey, A. Dalke, K. Schulten, VMD: Visual molecular dynamics. *J. Mol. Graph.* **14**, 33–38 (1996).
64. N. Michaud-Agrawal, E. J. Denning, T. B. Woolf, O. Beckstein, MDAnalysis: A toolkit for the analysis of molecular dynamics simulations. *J. Comput. Chem.* **32**, 2319–2327 (2011).
65. J. Wang, R. M. Wolf, J. W. Caldwell, P. A. Kollman, D. A. Case, Development and testing of a general amber force field. *J. Comput. Chem.* **25**, 1157–1174 (2004).
66. W. L. Jorgensen, J. Chandrasekhar, J. D. Madura, R. W. Impey, M. L. Klein, Comparison of simple potential functions for simulating liquid water. *J. Chem. Phys.* **79**, 926–935 (1983).
67. I. S. Joung, T. E. Cheatham III, Determination of alkali and halide monovalent ion parameters for use in explicitly solvated biomolecular simulations. *J. Phys. Chem. B* **112**, 9020–9041 (2008).
68. U. Essmann, L. Perera, M. L. Berkowitz, T. Darden, H. Lee, L. G. Pedersen, A smooth particle mesh Ewald method. *J. Chem. Phys.* **103**, 8577–8593 (1995).
69. B. Hess, H. Bekker, H. J. C. Berendsen, J. G. E. M. Fraaije, LINCS: A linear constraint solver for molecular simulations. *J. Comput. Chem.* **18**, 1463–1472 (1997).
70. S. Nosé, A molecular dynamics method for simulations in the canonical ensemble. *Mol. Phys.* **52**, 255–268 (1984).
71. W. G. Hoover, Canonical dynamics: Equilibrium phase-space distributions. *Phys. Rev. A* **31**, 1695–1697 (1985).
72. F. Eisenhaber, P. Lijnzaad, P. Argos, C. Sander, M. Scharf, The double cubic lattice method: Efficient approaches to numerical integration of surface area and volume and to dot surface contouring of molecular assemblies. *J. Comput. Chem.* **16**, 273–284 (1995).
73. S. O. Yesylevskyy, L. V. Schafer, D. Sengupta, S. J. Marrink, Polarizable water model for the coarse-grained MARTINI force field. *PLOS Comput. Biol.* **6**, e1000810 (2010).
74. J. Wohlert, O. Edholm, Dynamics in atomistic simulations of phospholipid membranes: Nuclear magnetic resonance relaxation rates and lateral diffusion. *J. Chem. Phys.* **125**, 204703 (2006).
75. S. J. Marrink, A. H. De Vries, A. E. Mark, Coarse grained model for semiquantitative lipid simulations. *J. Phys. Chem. B* **108**, 750–760 (2004).
76. G. R. Bowman, V. S. Pande, F. Noé, *An Introduction to Markov State Models and Their Application to Long Timescale Molecular Simulation* (Springer Science & Business Media, 2014), vol. 797.
77. J. Weng, M. Yang, W. Wang, X. Xu, Z. Tian, Revealing thermodynamics and kinetics of lipid self-assembly by Markov State Model analysis. *J. Am. Chem. Soc.* **142**, 21344–21352 (2020).
78. K. A. Beauchamp, G. R. Bowman, T. J. Lane, L. Maibaum, I. S. Haque, V. S. Pande, MSMBuilder2: Modeling conformational dynamics at the picosecond to millisecond Scale. *J. Chem. Theory Comput.* **7**, 3412–3419 (2011).
79. M. P. Harrigan, M. M. Sultan, C. X. Hernández, B. E. Husic, P. Eastman, C. R. Schwantes, K. A. Beauchamp, R. T. McGibbon, V. S. Pande, MSMBuilder: Statistical models for biomolecular dynamics. *Biophys. J.* **112**, 10–15 (2017).

Acknowledgments

Funding: This work was supported by National Key R&D Program of China (2022YFB3804600), the National Natural Science Foundation of China (U22A20156, 32171319, 31971297, 52073102, 22073090, 21991132, and 52021002), Guangdong Provincial Pearl River Talents Program (2019QN01Y090), Guangdong Basic and Applied Basic Research Foundation (2023B1515020086), the Natural Science Foundation of Guangdong Province (2019A1515010739 and 2021A1515010283), the Foundation of Guangzhou Science and Technology Bureau (202201020302 and 202102010298), and USTC Tang Scholar. **Author contributions:** Conceptualization: M.X., Y.B., and Y.L. Investigation: Y.L., Y.Z., J.C., X.Z., B.H., S.H., C.L., S.J., P.Z., Y.Y., H.Z., and Y.W. Simulation studies: Y.H. and S.X. GUV study and single-molecule fluorescence imaging: C.X. and B.Y. SAXS studies: Z.G. and X.D. Supervision: M.X., Y.B., and S.X. Writing—original draft: Y.L., Y.B., Y.H., S.X., and M.X. Writing—review and editing: Y.L., Y.B., S.X., and M.X. **Competing interests:** The authors declare that they have no competing interests. **Data and materials availability:** All data needed to evaluate the conclusions in the paper are present in the paper and/or the Supplementary Materials.

Submitted 9 January 2024
Accepted 25 July 2024
Published 30 August 2024
10.1126/sciadv.adn9435